A&A, 712, L26 (2026)
https://doi.org/10.1051/0004-6361/202661603
© The Authors 2026

Astronomy & Astrophysics

LETTER TO THE EDITOR

Unmasking (44) Nysa: Evidence for a trilobate structure

K. Minker, A. Berdeu, G. Li Causi, J. Hanuš, M. Marsset, A. Conrad, F. Pedichini, S. Antoniucci, et al.

(Full author list and affiliations details can be found after the references)

Received 22 June 2026 / Accepted 24 July 2026

ABSTRACT

Context. (44) Nysa is one of the largest known E-type asteroids. Light curve inversion models have indicated that it may have an elongated shape commonly found in large binary systems.

Aims. We aimed to identify the morphology and presence of possible satellites orbiting Nysa.

Methods. We observed Nysa with the visible-wavelengths adaptive-optics instruments SHARK-VIS and SPHERE/ZIMPOL in order to image the object with the highest possible spatial resolution and visually identified surface features on the object. A shape model was constructed from these images and photometric light curves using the ADAM code.

Results. Imaging revealed a highly unusual morphology with multiple distinct surface features, including two distinct valleys that are most easily interpreted as colli. A faint satellite was identified in the deconvolution residuals in multiple datasets.

Conclusions. We determine that (44) Nysa is a binary system most likely consisting of a contact-trinary or highly-irregular, coherent primary object and a small satellite.

Key words. instrumentation: adaptive optics – minor planets, asteroids: individual: (44) Nysa

1. Introduction

Asteroid (44) Nysa was named to honor the mythical land of Nysa where the god Dionysus (also known as Bacchus) was raised by nymphs (Schmadel 2012), or perhaps the Nymph that raised him[1]. Dionysus is associated with masks and theater, known for concealing his true nature. The naming of Nysa for the land in which this god of illusion was raised is quite fitting, as asteroid Nysa has long managed to evade attempts to identify its true nature, leaving only vague clues to the object's structure. Nysa was observed with the *Hubble* Space Telescope's Fine Guidance Sensor, by radar from Arecibo Observatory, and by stellar occultation, which collectively identified a potential concavity or bilobate structure, but no concrete determination of the asteroid's morphology was achieved through these efforts (Tanga et al. 2002; Shepard et al. 2008; Herald et al. 2019). A light curve inversion model for Nysa's shape suggested an elongated morphology typical of binary systems with large primaries (Kaasalainen et al. 2002; Carry et al. 2021; Minker et al. 2025).

Nysa is one of the largest known E-type asteroids (Mahlke et al. 2022), and the brightest as the only E-type with $H < 7$. This rare taxonomic type is associated with enstatite-rich meteorites, including aubrites and enstatite chondrites (Zellner et al. 1977; Keil 2010) and is thought to be formed from the same feedstocks as terrestrial planets. As defined by Clark et al. (2004), Nysa-like E-types form a subcategory of this compositional group, which exhibit additional orthopyroxene features. These objects do not provide a clear spectroscopic match to any known meteorites, although this complex problem may be biased by grain size effects and other influences (e.g., Cantillo et al. 2026). The Nysa-like spectroscopic profile has been detected in small near-Earth asteroids (NEAs; e.g., Reddy et al. 2016), including most recently the future Hayabusa2# target 1998 KY_{26} (Tatsumi et al. 2026).

[1] Natur und Offenbarung, 1857.

Nysa's large size and high albedo (reports range from 0.41–0.55, see Berthier et al. 2023, and references within) position the asteroid as a particularly attractive observational target. As a result, it was one of the first asteroids to have a rotation period measured by photometric light curve (e.g., Bianchi & Padova 1920). Nysa shows both a higher polarization ratio ($\mu = 0.50 \pm 0.02$) and radar albedo (0.19 ± 0.06) compared to the majority of main-belt asteroids, suggesting a high surface bulk density (Shepard et al. 2008).

Recent observations by SHARK-VIS on the Large Binocular Telescope (LBT) managed to reveal the highly unusual morphology of (44) Nysa (Minker et al. 2026). These observations and their interpretation are discussed in the remainder of this Letter.

2. Observations

2.1. Adaptive optics imaging

We observed Nysa with SHARK-VIS (Pedichini et al. 2022, 2024) in UT 2026-02-15 and UT 2026-03-21 (program AZ-2026A-004 and DDT), and with VLT/SPHERE/ZIMPOL (Beuzit et al. 2019; Schmid et al. 2018) (program 116.2AQK.001) in ten epochs between 2026-03-09 and 2026-04-05. SHARK-VIS acquired images at the F/15 Nasmyth focal plane of the LBT after atmospheric correction by the SOUL adaptive optics (AO) system (Pinna et al. 2016). On UT 2026-02-15 we acquired DIT = 25 ms exposure frame sequences with the R_{Bessel} filter between UT 04:20 and UT 07:44 with seeing conditions stable at 0.8″. On 2026-03-21 we acquired DIT = 80 ms exposures alternating between R_{Bessel} and V_{Bessel} filters between UT 02:34 and UT 05:57 with seeing variable between 0.8–1.1″. Both acquisitions used a field stop with a diameter of 1.2″. The plate scale was 6.43 mas/px on the first date, while on the second date an internal magnification

Open Access article, published by EDP Sciences, under the terms of the Creative Commons Attribution License (https://creativecommons.org/licenses/by/4.0), which permits unrestricted use, distribution, and reproduction in any medium, provided the original work is properly cited.
This article is published in open access under the Subscribe to Open model. Subscribe to A&A to support open access publication.

lens yielded an effective plate scale of ≈4.45 mas/px to better sample the image. Additional details can be found in Table C.1.

The ZIMPOL dataset consists of ten identical sequences of images in the N_R, V, Cnt748, and Cnt820 filters, recorded as two sets of two simultaneously imaged filters (N_R & V, Cnt748 & Cnt820). The ten observations were timed to cover the full rotation period and phase angles ranging from 21.6–27.1°. Each set of images included six 15 s exposures, for a total of 90 s exposure time per filter. Seeing ranged between 0.3–0.8″ for different epochs of observation. The timing and orbital geometry of these observations can be found in Table C.2.

The two imaging datasets were then processed with dark, flat, and cosmic ray correction, lucky imaging (in the case of the LBT observations), and blind deconvolution algorithms to maximize image quality and improve the visibility of surface features across the primary object. The techniques used for the reduction of these images can be found in Appendix B. The final processed video can be found in Visualization 1 (online video).

2.2. Photometric light curves

Photometric light curve observations were used to supplement the imaging dataset. Light curves were acquired at the 0.6 m TRAPPIST-North and -South telescopes (Jehin et al. 2011), BSA Observatory, the 0.5 m telescope at Robinson Observatory, and the 0.32 m telescope at Command Module Observatory. Some light curves were collected in multiple filters to search for color variation across Nysa's rotation period. Archival observations were collected from the Asteroid Lightcurve Photometry Database[2] (ALCDEF, Warner 2016). Most photometric light curve observations depict only small deviations from a sinusoid, although some present a singular flat minimum, as is typical of contact binaries and previously reported by Cellino et al. (1985). A summary of the photometric dataset can be found in Table C.3, and is illustrated alongside synthetic light curves produced from the shape model discussed in Sect. 3.

3. Shape model

A three-dimensional shape model of Nysa was reconstructed with the All-Data Asteroid Modeling algorithm (ADAM; Viikinkoski et al. 2015), combining the disk-resolved images described in Sect. 2.1 with the photometric light curves in Sect. 2.2. Nysa's rotation period, close to 6.42 h, has been known since the 1920s and has been subsequently confirmed and refined by several studies (e.g., Bianchi & Padova 1920; Groeneveld & Kuiper 1954). Previous light curve-based spin-state analyzes generally reported the usual mirror pole ambiguity, with solutions near ecliptic coordinates $(\lambda, \beta) \approx (100°, 60°)$ and $(280°, 60°)$ (e.g., Magnusson 1983; Taylor & Tedesco 1983). By contrast, the convex light curve inversion model of Kaasalainen et al. (2002) yielded a unique pole solution near $(99°, 58°)$. Our disk-resolved images clearly confirm this solution.

We followed the ADAM modeling strategy previously applied in several SPHERE-based studies, for example, for asteroids (16) Psyche (Viikinkoski et al. 2018), (7) Iris (Hanuš et al. 2018), and (31) Euphrosyne (Yang et al. 2020), as well as in the survey summary by Vernazza et al. (2021). The convex spin-state solution was adopted as the initial guess, ensuring convergence to the correct minimum. This solution, derived from the full set of available light curves, is close to that reported by Kaasalainen et al. (2002). We first computed a low-resolution model with 400 vertices and 800 facets, and then gradually increased the surface resolution while monitoring convergence and the reproducibility of topographic features by adjusting the regularization terms. Our final model, with 1600 vertices and 3200 facets, provides a good fit to both the observed light curves and all disk-resolved images. Further increasing the resolution does not improve the fit. The solution is stable with respect to changes in surface resolution, data weighting, and reasonable variations of the regularization parameters. Our ADAM configuration includes a regularization term that forces the calculated center of mass of the shape model to be as close as possible to the center of the coordinate system. Therefore, no information about the internal mass distribution can be derived from the model.

We also tested the consistency of the model against three stellar occultations with at least four chords (2007-01, 2017-09, 2017-10), reduced using the `Occult` software package[3]. Because the number of chords is limited and the sampled silhouettes are sparse, these occultations were not included directly in the shape reconstruction. Nevertheless, they are consistent with our preferred model and thus provide an independent validation of the solution (Fig. D.3).

The derived spin-state parameters determine spin-pole coordinates of $(\lambda, \beta) = (102.7 \pm 0.5°, 55.3 \pm 0.5°)$, a rotation period of $P = 6.4214175 \pm 0.0000005)$ h, and a volume-equivalent diameter of $D = 75^{+3}_{-1}$ km. A comparison between the shape model and the AO images as well as the fits to the light curves can be found in Fig. D.1.

4. Surface features

This dataset revealed a number of surface features across Nysa. Features were divided into two categories: indentations on the edges of the object and valleys or shadows on the center of the object. All features reported here are consistent with the rotation of the object and most are detected on multiple nights.

A map of identified surface features can be found in Figure E.1. We identified eleven notable features in the imaging dataset: eight edge indentations and two valleys. The valleys are most visible in higher phase-angle observations from the March dataset; this can be seen in Figure 1. The valleys appear when the asteroid is in an on-sky East-facing or West-facing geometry (see Fig. 1), suggesting that they transect the full circumference of the asteroid along its narrowest axis and join edge indentations on either side. We interpret these valleys as colli (necks) joining contact-fragments. The E-I-F (see Fig. 1, Fig. E.1, and Table E.1) collum joins the two main lobes of Nysa, while the E-J-A collum separates the two halves of the smaller lobe. In this interpretation, and taking all remaining edge indentations to be craters, we identify three lobes, two colli, and five craters.

Tupieva (2003) identified a *U-B* color variation throughout Nysa's rotation. We observed no color variation through multifilter light curves or between lobes in the SPHERE dataset at more than a 5% level, well below the variation of 0.2 mag reported by Tupieva (2003).

5. S/2026 (44) 1

A small satellite was identified in the LBT observations from 2026-02-15 and 2026-03-21 (Berdeu et al. 2026). The satellite was detected both (I) in the residuals of the blind deconvolutions that model and subtract the bright halo around Nysa and

[2] https://alcdef.org/

[3] http://www.lunar-occultations.com/iota/occult4.htm

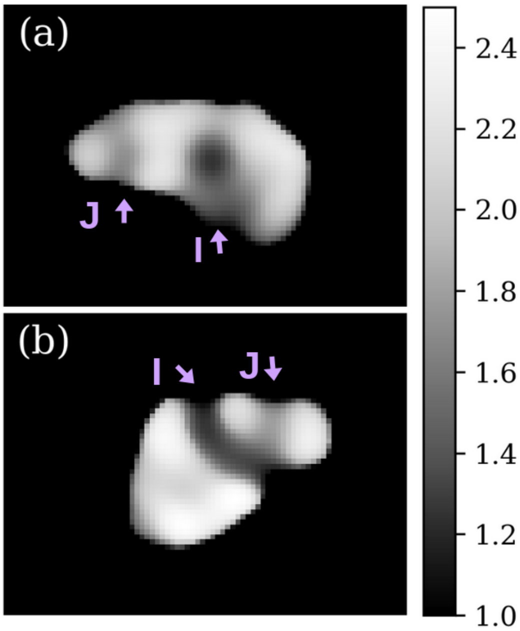

Fig. 1. 2026-03-21 SHARK-VIS observations of Nysa; color scale shows relative brightness and is tuned to enhance the visibility of shadows, indicative of surface indentations or valleys in the sky: East-facing (upper panel) and West-facing (lower panel) geometries. Two clear shadowed regions can be seen, one at the object's center (I) and another close to its narrowest point (J). Shadows are apparent in multiple geometries, appear to fully encircle the asteroid, and are bounded by edge indentations. This suggests that both are colli connecting a total of three lobes. Additional features are annotated in Fig. E.1.

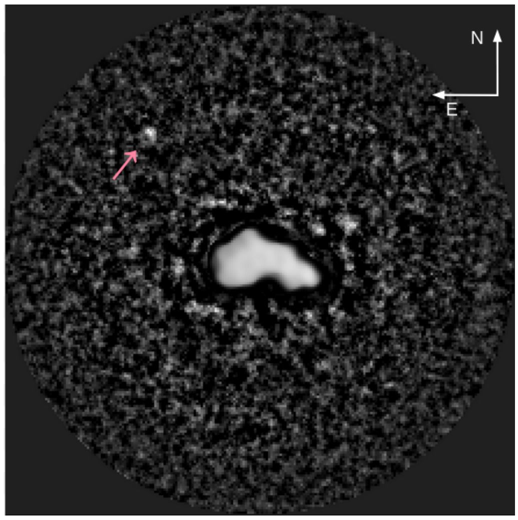

Fig. 2. Residuals of *R*-band images of the Nysa system on 2026-02-15 after processing with the blind deconvolution method of Appendix B.3. The position of the satellite is marked with a pink arrow. To improve the S/N, the deconvolution residuals were averaged with a a ±5 frame sliding window. To provide scale, the primary has been superimposed. The associated movies for this date (panel a) and 2026-03-21 (panel b) are available online.

(II) from an independent principal component analysis (PCA) – angular differential imaging (ADI) analysis inspired by exoplanet detection (see Sects. B.3 and B.4 and Figs. B.1 and B.2).

The identified point source was clearly moving on sky with the trajectories depicted in Fig. B.1 while remaining present in a Nysa-centered frame for over three hours in each epoch. This removes the possibility of contamination from a background object. The satellite was detected at a projected separation of 180 km and 170 km in the February and March observations, respectively. A $\Delta_{\rm mag} \approx 9$ was measured between components. Assuming a consistent albedo between components, this provides a satellite diameter of $D_s = 1 \pm 0.5$ km. The orbital scale with respect to the primary size is demonstrated in Fig. 2. An additional study of this satellite will be reported in future work.

6. Discussion

6.1. Atypical morphology

Several critical constraints restrict possible formation mechanisms for Nysa's abnormal morphology:

- The mechanism should not require the ejection of a large amount of material in Nysa's current position. Although Nysa is embedded in the expansive Nysa-Polana complex (Cellino et al. 2001), only a small fraction of the material in this complex exhibits an albedo high enough to indicate enstatite material (Brož et al. 2024; Tatsumi et al. 2026). Neither the total quantity nor size of individual fragments of high-albedo material in the Nysa-Polana complex is sufficient to indicate a recent dramatic reshaping of the object.
- Dispersed Nysa-like E-type asteroids are observed scattered throughout the main belt (Clark et al. 2004), as well as in NEA populations (Reddy et al. 2016; Tatsumi et al. 2026), so a formation event that occurs prior to implantation in the main belt could explain the lack of a dynamical center for the Nysa-like material that would be expected from a recent formation.
- Ideally, the mechanism should provide a possibility of low-velocity mergers and/or re-accumulation of material from a single parent body. Nysa displays at least two deep valleys that circumscribe the object. Our preferred interpretation of these features is that they are colli connecting three distinct lobes. Nysa's surface composition, representing only a fraction of the already rare E-type asteroids (the "Nysa-like" subset Clark et al. 2004), shows no color or albedo difference between lobes of the object in the observed filters. This suggests that all surface material on Nysa came from the same parent body and by extension, that all of the lobes should be sourced from the said parent body.

We present possible scenarios for the origin of Nysa's highly unusual shape in the following subsections.

6.1.1. Battering

The simplest explanation for Nysa's unusual morphology is that Nysa is a heavily battered object that originated from a singular object that has been heavily deformed due to substantial cratering. If this interpretation is correct, Nysa must have a sturdy interior to survive these nearly catastrophic collisions. The cratering events may not be ongoing, as very little enstatite material is observed in Nysa's orbital neighborhood. The detection of a very high density ($\rho \gtrapprox 5\,{\rm g.cm^{-3}}$) could support, but not necessarily confirm, this possibility by suggesting the presence of a rigid iron-rich core which could support this distorted morphology. This mechanism does not adequately explain the presence of the two valleys that transect Nysa's surface along its narrowest axis and is therefore not our preferred explanation. Alternatively, it could be possible that Nysa is a single coherent planetary shard whose bizarre shape originates from impact-based reshaping along preexisting fractures. In this scenario, the battering would be responsible solely for the smaller concavities on the object. A lower aubrite-like density (3−4 g.cm^{-3}) would be expected.

6.1.2. Contact trinary

A second explanation is that Nysa is a composite of several components in a contact trinary (or more) configuration. This formation possibility is supported by the presence of multiple circum-asteroid valleys across Nysa's narrowest axis, typically interpreted as a collum joining two distinct components as a contact binary (e.g., Toutatis, Zhu et al. 2014). In some cases, a dramatic indentation can be found in the collum, with little evidence of relaxation over time, as is the case for (486958) Arrokoth (Stern et al. 2019). Nysa is notably larger than any of these objects, and the central concavity is much more extreme than any previously observed. Therefore, this interpretation indicates that Nysa would need to be sturdy enough to maintain its seemingly unstable structure through the small impacts over the object's lifetime and possibly implantation to the main belt. Alternatively, it could be possible that the three components of Nysa are individually strong, but their specific configuration has varied over time as the system has been disrupted. Although most well-studied asteroids have fairly low cohesion, if Nysa and its sub-components possess higher cohesion, it may be easier for Nysa to retain its unusual shape over time, as this material would be more likely to retain an irregular shard-like topography after impacts (e.g., Keller et al. 2010). In future work, a further analysis of the long-term stability of the system will be presented.

6.2. Formation

Various proposed mechanisms could cause the observed structure. However, we note that Nysa does indeed match the elongated, lopsided, fast-rotating profile associated with large binary primaries (Carry et al. 2021; Minker 2025). It is possible that the shape originates from a "hit-and-run collision" as described by Asphaug et al. (2006). This process has been proposed to significantly deform differentiated asteroids as tidal stresses affect the lower density mantle layer more strongly than the dense core, and are capable of stripping an object into similar-sized fragments ("string-of-pearls") (Asphaug et al. 2006). Nysa could be an accumulation of such fragments shortly after the initial deformation reassembled via low-velocity merger (e.g., Raducan et al. 2025), explaining apparent surface homogeneity.

The possibility of re-accumulation following a giant impact to a proto-Nysa cannot be excluded. However, it seems unlikely that such a re-accumulation could occur in situ. An impact capable of creating three 60–20 km-sized objects that then re-accumulate should also produce additional debris, which would be observed as a large, enstatite-rich dynamical family of which Nysa is the largest member. This family has not been detected (Dykhuis & Greenberg 2015).

7. Conclusions

Observing (44) Nysa with adaptive optical-wavelength imaging, we were able to identify both a contact-trinary morphology and a small satellite. The origin of this structure is not yet clear, but it may have originated prior to Nysa's implantation to the main belt due to the lack of enstatite material in the dynamical space surrounding Nysa. Ongoing work on the satellite dynamics will provide a refined density constraint, and together with modeling of the long-term stability and formation of the Nysa system will reveal additional clues to the object's internal structure and origin.

Data availability

Movies associated with Fig. 2 and with Sect. 2.1 are available at `https://www.aanda.org`

References

Amara, A., & Quanz, S. P. 2012, MNRAS, 427, 948
Asphaug, E., Agnor, C. B., & Williams, Q. 2006, Nature, 439, 155
Berdeu, A. 2024, A&A, 688, A18
Berdeu, A., & Soulez, F. 2025, AO4ELT8, Viña Del Mar, Chile
Berdeu, A., Minker, K., Li Causi, G., et al. 2026, CBETs, 5693, 1
Berthier, J., Carry, B., Mahlke, M., & Normand, J. 2023, A&A, 671, A151
Beuzit, J.-L., Vigan, A., Mouillet, D., et al. 2019, A&A, 631, A155
Bianchi, E., & Padova, E. 1920, Mem. Soc. Astron. It., 1, 39
Brož, M., Vernazza, P., Marsset, M., et al. 2024, A&A, 689, A183
Cantillo, D. C., Pearson, N. C., Ridenhour, K. I., et al. 2026, Planet. Sci. J., 7, 151
Carry, B., Vernazza, P., Vachier, F., et al. 2021, A&A, 650, A129
Cellino, A., Pannunzio, R., Zappala, V., Farinella, P., & Paolicchi, P. 1985, A&A, 144, 355
Cellino, A., Zappalà, V., Doressoundiram, A., et al. 2001, Icarus, 152, 225
Charbonnier, P., Blanc-Feraud, L., Aubert, G., & Barlaud, M. 1997, IEEE Trans. Image Process., 6, 298
Clark, B. E., Bus, S. J., Rivkin, A. S., et al. 2004, J. Geophys. Res., 109, E02001
Durech, J., Sidorin, V., & Kaasalainen, M. 2010, A&A, 513, A46
Dykhuis, M. J., & Greenberg, R. 2015, Icarus, 252, 199
Freudling, W., Zampieri, S., Coccato, L., et al. 2024, A&A, 681, A93
Groeneveld, I., & Kuiper, G. P. 1954, ApJ, 120, 529
Hanuš, J., Vernazza, P., Viikinkoski, M., et al. 2018, AAS/Division for Planetary Sciences Meeting Abstracts #50, 50, 404.06
Herald, D., Frappa, E., Gault, D., et al. 2019, Asteroid Occultations V3.0, NASA Planetary Data System, Asteroid Occultations V3.0. urn:nasa:pds:smallbodiesoccultations::3.0
Jehin, E., Gillon, M., Queloz, D., et al. 2011, Messenger, 145, 2
Kaasalainen, M., Torppa, J., & Piironen, J. 2002, A&A, 383, L19
Keil, K. 2010, Chem. Erde / Geochem., 70, 295
Keller, H. U., Barbieri, C., Koschny, D., et al. 2010, Science, 327, 190
Magnusson, P. 1983, in Asteroids, Comets, and Meteors, eds. C.-I. Lagerkvist, & H. Rickman, 77
Mahlke, M., Carry, B., & Mattei, P.-A. 2022, A&A, 665, A26
Marois, C., Lafrenière, D., Doyon, R., Macintosh, B., & Nadeau, D. 2006, ApJ, 641, 556
Minker, K. 2025, Ph.D. Thesis, Université Côte d'Azur
Minker, K., Carry, B., Vachier, F., et al. 2025, A&A, 701, A42
Minker, K., Conrad, A., Pedichini, F., et al. 2026, CBETs, 5664, 1
Pedichini, F., Piazzesi, R., Viavattene, G., et al. 2022, SPIE Conf. Ser., 12185, 121856Q
Pedichini, F., Piazzesi, R., Li Causi, G., et al. 2024, SPIE Conf. Ser., 13097, 130970A
Pinna, E., Esposito, S., Hinz, P., et al. 2016, SPIE Conf. Ser., 9909, 99093V
Raducan, S. D., Madeira, G., Agrusa, H. F., et al. 2025, Nat. Commun., 16, 11033
Reddy, V., Sanchez, J. A., Bottke, W. F., et al. 2016, AJ, 152, 162
Schmadel, L. D. 2012, Dictionary of Minor Planet Names (Berlin, Heidelberg: Springer)
Schmid, H. M., Bazzon, A., Roelfsema, R., et al. 2018, A&A, 619, A9
Shepard, M. K., Kressler, K. M., Clark, B. E., et al. 2008, Icarus, 195, 220
Soummer, R., Pueyo, L., & Larkin, J. 2012, ApJ, 755, L28
Stern, S. A., Weaver, H. A., Spencer, J. R., et al. 2019, Science, 364, aaw9771
Tanga, P., Hestroffer, D., Cellino, A., et al. 2002, ESA SP, 500, 517
Tatsumi, E., de León, J., & Popescu, M. M. 2026, A&A, 709, A105
Taylor, R. C., & Tedesco, E. F. 1983, Icarus, 54, 13
Tupieva, F. A. 2003, A&A, 408, 379
Vernazza, P., Ferrais, M., Jorda, L., et al. 2021, A&A, 654, A56
Viikinkoski, M., Kaasalainen, M., & Durech, J. 2015, A&A, 576, A8
Viikinkoski, M., Vernazza, P., Hanuš, J., et al. 2018, A&A, 619, L3
Warner, B. D. 2016, Minor Planet. Bull., 43, 26
Yang, B., Hanuš, J., Carry, B., et al. 2020, A&A, 641, A80
Zellner, B., Leake, M., Morrison, D., & Williams, J. G. 1977, Geochim. Cosmochim. Acta, 41, 1759
Zhu, M.-H., Fa, W., Ip, W.-H., et al. 2014, Geophys. Res. Lett., 41, 328

Authors and affiliations

K. Minker[1,⋆], A. Berdeu[2,13,⋆], G. Li Causi[3], J. Hanuš[4], M. Marsset[5], A. Conrad[6], F. Pedichini[3], S. Antoniucci[3], P. Vaccari[3], N. Moskovitz[1], B. Carry[7], T. Polakis[8], M. Ferrais[9], E. Jehin[10], R. Bonamico[11], R. Hicks[9], D. Smith[9], M. A. Miftah[10,12], and E. Marini[3]

[1] Lowell Observatory, 1400 W. Mars Hill Rd., Flagstaff, AZ, USA
[2] European Southern Observatory (ESO), Santiago, Chile
[3] INAF-Osservatorio Astronomico di Roma, Via Frascati, 33, Monteporzio Catone 00078, Italy
[4] Charles University, Faculty of Mathematics and Physics, Institute of Astronomy, V Holešovičkách 2, 180 00 Prague, Czech Republic
[5] European Southern Observatory (ESO), Karl-Schwarzschild-Strasse 2, 85748 Garching bei München, Germany
[6] Large Binocular Telescope Observatory, Tucson, AZ, USA
[7] Université Côte d'Azur, Observatoire de la Côte d'Azur, Lagrange, CNRS, Nice, France
[8] Command Module Observatory, Tempe, AZ, USA
[9] Florida Space Institute, University of Central Florida, 12354 Research Parkway, Orlando, FL 32828, USA
[10] Space Sciences, Technologies & Astrophysics Research (STAR) Institute, University of Liège, Liège, Belgium
[11] BSA Osservatorio (K76), Strada Collarelle 53, 12038 Savigliano, Cuneo, Italy
[12] Cadi Ayyad University (UCA), Oukaimeden Observatory (OUCA), Faculté des Sciences Semlalia (FSSM), High Energy Physics, Astrophysics and Geoscience Laboratory (LPHEAG), Marrakech, Morocco
[13] LIRA, Observatoire de Paris, Université PSL, Sorbonne Université, Université Paris Cité, CY Cergy Paris Université, CNRS, 92190 Meudon, France

⋆ Corresponding authors: kminker@lowell.edu; Anthony.Berdeu@obspm.fr

Appendix A: Acknowledgements

Acknowledgements. K.M. acknowledges support through the Percival Lowell Postdoctoral Fellowship, which is funded in part through generous donations of the Percival Lowell Society. J.H. was supported by GACR grant no. 25-16789S of the Czech Science Foundation. We wish to thank Joseph Shields and the ESO DDT selection committee for the allocation of director's discretionary time to this project, Johan Olofsson and Jennifer Power for the observing support, Richard Jerousek and Christopher Duffey for their contributions to the Robinson Observatory. The LBT is an international collaboration among institutions in the United States and Europe. At the time data were acquired for this research, LBT Corporation Members were the University of Arizona on behalf of the Arizona Board of Regents; Istituto Nazionale di Astrofisica, Italy; and The Ohio State University, representing The Ohio State University, University of Notre Dame, University of Minnesota, and University of Virginia. This research used the facilities of the Italian Center for Astronomical Archives (IA2) operated by INAF at the Astronomical Observatory of Trieste. Observations have benefited from the use of ALTA Center (alta.arcetri.inaf.it) forecasts performed with the Astro-Meso-Nh model. Initialization data of the ALTA automatic forecast system come from the General Circulation Model (HRES) of the European Centre for Medium Range Weather Forecasts. TRAPPIST is funded by the Belgian F.R.S.-FNRS under grant PDR T.0120.21, and TRAPPISTNorth is funded by the University of Liège in collaboration with Cadi Ayyad University of Marrakech. EJ is Director of Research at the Belgian National Fund for Scientific Research (F.R.S.-FNRS). Thank you to E. Asphaug, A. Thirouin, and M. Goldberg for the constructive discussion.

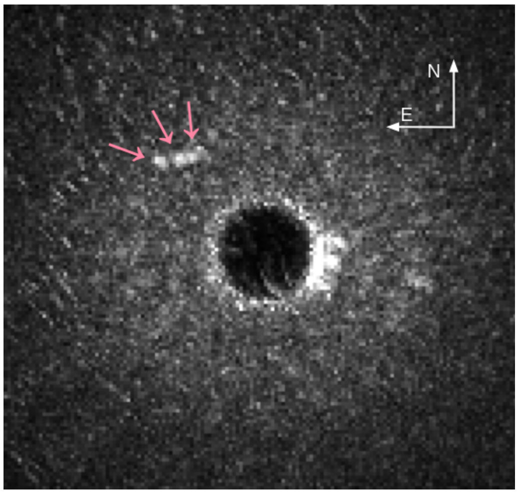

Fig. B.1. Maximum pixel stack of PCA-ADI treated R-band images of the Nysa system on 2026-02-15, three detected positions of the moon on this night are superimposed and marked with pink arrows.

Appendix B: Adaptive optics data reduction

B.1. Raw data reduction

We processed the SHARK-VIS frames with the custom DReAMS (Data Reduction, Analysis, and Modeling for SHARK-VIS) pipeline (Li Causi et al., in prep). The raw frames were reduced through various steps to correct for detector signatures: (I) subtraction of a cleaned average dark image, separately acquired at the end of the observing night; (II) correction of the frame-by-frame variable bias pattern, mainly consisting of non-static column-by-column (and less intense row-by-row) bias variations, which we measured on each frame as the column and row averages, respectively, of the pixels outside the field stop; (III) cosmic ray flagging; (IV) division by a flat field map, interpolated from a flat field ramp previously acquired in the instrument calibration phase.

The SPHERE observations were obtained in imaging mode and processed using the standard ZIMPOL imaging pipeline through the ESO Data Processing System (EDPS; Freudling et al. 2024). The pipeline performs standard calibrations including flat-field correction, bad-pixel identification, and image orientation. To enable high-precision polarimetric observations, ZIMPOL employs a masked CCD synchronized with a fast polarization modulator. In non-polarimetric imaging, this results in one row out of two not being used. To recover a uniform pixel sampling, the reduction pipeline reconstructs the final image by interpolating across these masked rows. This reconstruction process can leave low-level striping artifacts visible in the deconvolved images (see Fig. D.2).

B.2. Pre-processing SHARK-VIS short exposures

The idea behind the SHARK-VIS short exposures was to freeze the turbulence and the residual jitter from the AO system to increase image quality. Nonetheless, taken individually, they are too noisy and need to be adequately stacked. We implemented two different strategies depending on the science need.

B.2.1. Nysa's shape: lucky imaging and super-resolution

For Nysa's imaging and shape recovery, the sharpest possible images are needed. As pre-processing for the blind deconvolution of Sect. B.3, we performed lucky imaging. We split the exposures in batches of 2 minutes, corresponding to 4800 (resp. 1500) frames for the dataset of UT 2026-02-15 (resp. UT 2026-03-21) to limit the motion blur due to Nysa's proper rotation and the evolution of the parallactic angle. The frames were sorted by their sharpness computed via total-variation (Charbonnier et al. 1997) and then co-aligned on Nysa's photocenter. Then, this alignment was iteratively refined in the resulting stacked image, iterating thrice. The sub-pixel alignment and stacking was done via linear interpolation.

We kept the best 2.5 % of frames for the UT 2026-02-15 night. To compensate the loss of one magnitude due to Nysa's farther distance and the optical magnification while keeping a similar S/N, we kept 20 % of the best frames for the UT 2026-03-21 night.

Finally, for the UT 2026-02-15 dataset, the interpolation grid was defined with a resolution twice as high as the pixel pitch to perform numerical super-resolution via the dithering induced by the residual AO jitter. Figure B.2a gives an example of a stacked batch of 2 minutes, while Fig. B.2b shows its corresponding lucky imaging reduction with the factor of two resolution enhancement. As the UT 2026-03-21 dataset was obtained with optical magnification, we did not super-resolve the reduced frames.

B.2.2. Moon detection: co-alignment of all frames

For companion detection, the highest possible S/N is needed. As pre-processing for the PCA-ADI analysis described in Sect. B.4, we used the full dataset regardless of image quality, in order to increase the signal to noise ratio. Individual frames were aligned on Nysa's photocenter. Their sub-pixel alignment was performed with a fast Fourier transform translation.

B.3. Blind deconvolution algorithm

To deconvolve the different datasets (the long exposure ZIMPOL data, see Sect. B.1 and the SHARK-VIS stacked frames after lucky imaging, see Sect. B.2.1), we followed the method of Berdeu (2024), upgraded with a better segmentation of the asteroid described by Berdeu & Soulez (2025). The method performs a blind deconvolution of the images, jointly recovering (I) the de-blurred image of the asteroid, see Fig. B.2d and, (II) the AO PSF in its full complexity, see Fig. B.2e. Doing so allows for modeling the bright halo produced by the AO residuals and AO cutoff frequency visible in Fig. B.2c. Removing its model from the data highlights potential moons in the residuals, see Fig. B.2f. Finally, the deconvolved images were derotated by the parallactic angle into sky-coordinates.

We wish to draw the reader's attention to the high dynamics at play in this method. The reduced data peak to 4500 Analog to Digital Units (ADUs), while the halo spans on the full dynamic down to a few tens of ADUs. After the deconvolution by the extended PSF which is recovered across three orders of magnitude, the photometry of the asteroid jumps close to ≈10000 ADU while S/2026 (44) 1 hides below a 10 ADU level. This point-like source can be followed throughout the full sequence of the two nights (UT 2026-02-15 and 2026-03-21).

The resulting video from the LBT deconvolutions can be found in Visualization 1. Some individual LBT frames and the VLT observations can be found in Fig. D.2.

B.4. Principal Component Analysis

The SHARK-VIS data are pupil stabilized: the instrument PSF orientation is fixed with respect to the detector while the field rotates with the parallactic angle. This allowed us to adapt the angular differential imaging method classically used for exoplanet detection (ADI, Marois et al. 2006), in order to confirm the detection of the satellite with an independent approach. From the co-aligned frames of Sect. B.2.2 we computed an ADI based on principal component analysis (PCA-ADI, Amara & Quanz 2012; Soummer et al. 2012). It consists of subtracting from each frame its projection on a limited number of PCA bases (first 1000 components), then de-rotating the frames, and finally computing their average stack. Due to the fast orbital motion of the putative moon, we split these resulting frames in batches of 10000 before average stacking, thus obtaining a series of sequential stacks (40 batches for the first night, and 11 for the second night).

In sixteen of these resulting stacks for UT 2026-02-15 and three stacks for UT 2026-03-21, we confirmed the detection of a point-like source about 215 mas and 175 mas respectively from Nysa's center as seen in the blind deconvolution residuals. These stacks were consecutive during the portion of the night with the best seeing and therefore best AO performance. Figure B.1, which is the maximum value stack of these selected stacks, highlights the moon orbital motion which is clearly visible.

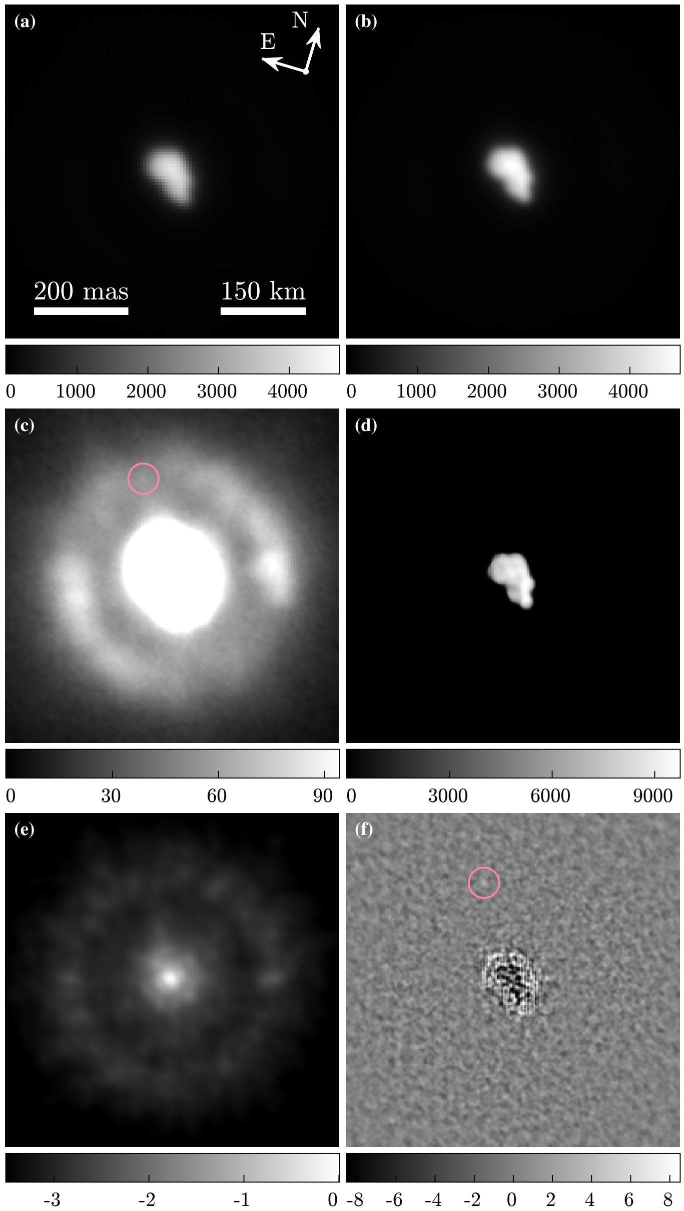

Fig. B.2. Applying the blind deconvolution algorithm on a SHARK-VIS 2 min batch of the UT 2026-02-15 night. Panel a: stack of batch. Panel b: lucky imaging and super-resolution of the 2 min batch, keeping the 2.5 % best frames. Panel c: saturated view of Panel b. Panel d: deconvolved image. Panel e: reconstructed PSF. Panel f: deconvolution residuals. Except for the PSF where the color scale is in log scale normalized to the PSF peak, all color scales are in ADU. The colored circle highlights Nysa's moon S/2026 (44) 1. The image orientation is in the pupil frame.

Appendix C: Supplementary tables

This appendix section contains additional tables describing the imaging datasets and photometric light curves.

Table C.1. Observing parameters for the LBT SHARK-VIS observations

UT	Filters	λ	Width (nm)	Exposure time	
				Total (hours)	Per frame (ms)
2026-02-15T04:20 to 07:44	R Bessel	645	140	3.3	25
2026-03-21T02:34 to 05:57	R Bessel	645	140	1.6	25
	V Bessel	533	77	1.6	80

Table C.2. Observing geometry during LBT/SHARK-VIS and VLT/SPHERE/ZIMPOL observations of (44) Nysa

Date	UT	Δ (au)	Phase angle (°)
2026-02-15*		1.14	12.7
2026-03-09	00:21	1.30	21.6
2026-03-11	01:58	1.32	22.3
2026-03-15	03:33	1.36	23.4
2026-03-16	03:33	1.37	23.7
2026-03-21*		1.43	24.8
2026-03-22	00:47	1.44	25.0
2026-03-22	02:15	1.44	25.0
2026-03-24	02:38	1.45	25.4
2026-04-01	01:23	1.54	26.7
2026-04-01	02:30	1.54	26.7
2026-04-05	01:30	1.59	27.1

Notes. Dates and observational geometry of Nysa during the imaging dataset. Dates marked with a * are SHARK-VIS observations, all others are SPHERE. Listed time marks the UT time during the first exposure. Observing geometry accessed from https://ssp.imcce.fr/forms/ephemeris

Table C.3. Date, duration ($\mathcal{L}$, in hours), number of points ($\mathcal{N}_p$), phase angle (α), filter(s), and observatory for each light curve.

Date	$\mathcal{L}$ (h)	$\mathcal{N}_p$	α (°)	Filt.	Obs.
2026-02-22	7.5	823	16.1	R	Robinson
2026-03-02	7.5	46	19.4	B,V,R,I	Command Mdl.
2026-03-04	6.3	90	20.1	B,V,R,I	Command Mdl.
2026-03-05	5.3	69	20.4	B,V,R,I	Command Mdl.
2026-03-05	5.1	114	20.4	R,B	Robinson
2026-03-06	5.1	187	21.0	R,B	Robinson
2026-03-07	6.6	257	21.3	R,B	Robinson
2026-03-10	2.7	123	22.0	L	Robinson
2026-03-14	4.3	292	23.3	RC	TRAPPIST-N
2026-03-15	4.2	198	23.6	CN	TRAPPIST-N
2026-03-16	3.3	147	23.8	C2	TRAPPIST-N
2026-05-19	2.9	267	27.3	R	TRAPPIST-S
2026-05-22	0.3	28	27.0	R	TRAPPIST-S
2026-05-24	2.7	248	26.9	R	TRAPPIST-S
2026-05-25	1.7	144	26.8	R	TRAPPIST-S

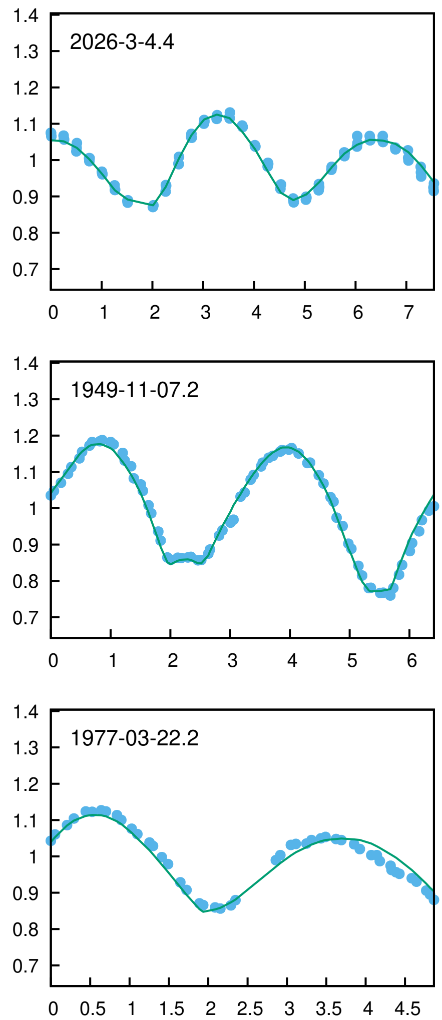

Fig. D.1. Comparison between the observed and synthetic light curves of asteroid (44) Nysa. Blue points correspond to disk-integrated photometric measurements, while green curves represent synthetic light curves computed from the final ADAM shape model. The horizontal axis shows the time from the beginning of each observing run in hours, and the vertical axis shows the relative intensity normalized to the mean brightness of the corresponding light curve. The observing epoch is indicated in the upper-left corner of each panel. The full sample of 83 light curve fits is available on DAMIT (Durech et al. 2010).

Appendix D: Shape model

This section contains information about the fit of Nysa's shape model as described in Sec. 3. Figure D.2 shows the fit of the model to the imaging dataset described in Sec. 2.1, and Fig. D.1 shows the fit of the model to the photometric light curves described in Sec. 2.2. Figure D.3 shows the fit of the shape model presented in Sec. 3 compared to historical occultation data. Information about the date, location, and observers of each occultation can be found in Table D.1. Figures D.2 and D.1 are representative of a more extensive dataset which can be found on DAMIT[4] (Durech et al. 2010). The shape model can also be downloaded at this location.

[4] https://damit.cuni.cz/projects/damit/

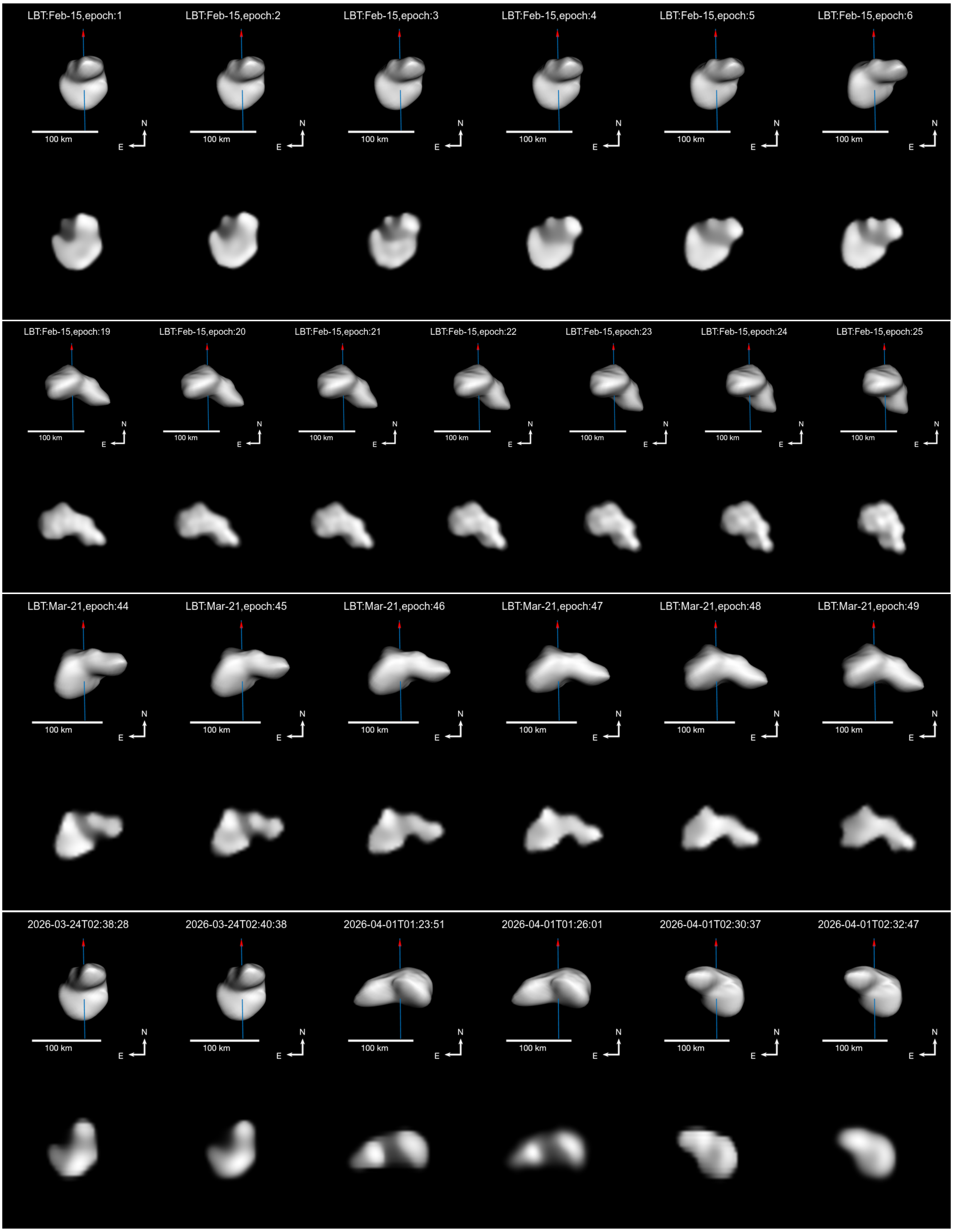

Fig. D.2. Comparison between the deconvolved images of (44) Nysa (lower rows) and the corresponding projections of the ADAM shape model (upper rows). The red arrows indicate the direction of the spin axis. The full dataset is available on DAMIT (Durech et al. 2010).

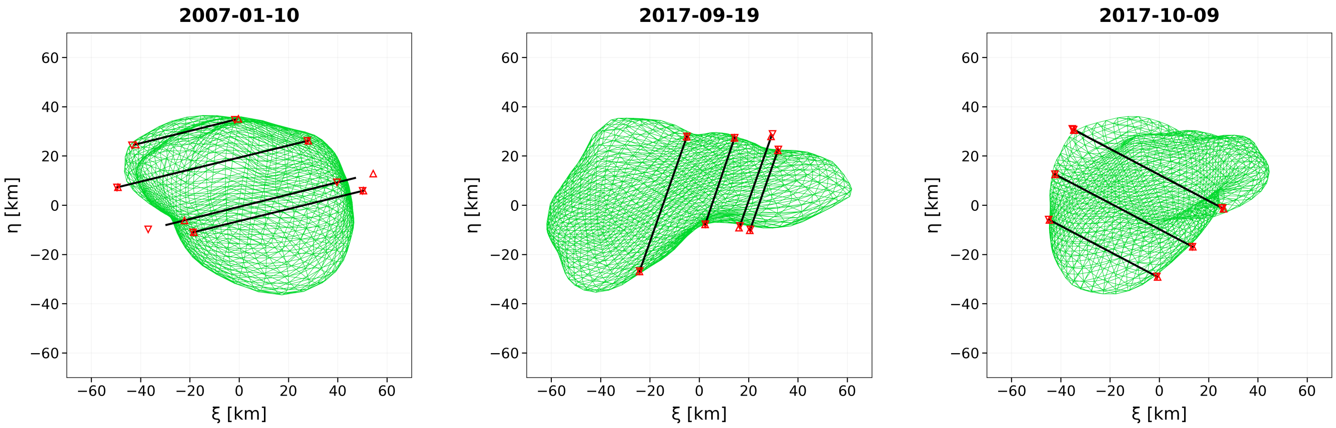

Fig. D.3. Observed occultation chords (black line segments) for three stellar occultations of Nysa, each with at least four positive chords, projected onto the sky plane, together with the final non-convex ADAM shape model (green mesh) at the corresponding rotational phases. The comparison is shown without any additional fitting. The close agreement confirms the validity of our size, shape, and spin-state solution.

Table D.1. Stellar occultation observations of asteroid (44) Nysa with more than three chords.

Observer	Location	λ (°)	ϕ (°)	h (m)	t_D (UTC)	σ_D (s)	t_R (UTC)	σ_R (s)	Type
				2007 January 10					
R. Venable	Clarks Hill, USA	−82.1876	+33.6677	128	01:30:47.3	–	–	–	M
P. Maley	Liberty City, USA	−94.9535	+32.4094	148	01:32:31.5	–	01:32:37.0	–	P
R. Venable	Harlem, USA	−82.3203	+33.4572	140	01:30:43.00	0.03	01:30:53.11	0.03	P
R. Nugent	Jacksonville, USA	−95.1576	+32.0615	100	01:32:28.8	1.00	01:32:38.9	1.00	P
R. Venable	Wrens, USA	−82.3811	+33.2240	137	01:30:43.91	0.02	01:30:52.92	0.02	P
				2017 September 19					
J. Rovira	Spain	−3.1619	+40.6052	753	03:28:52.78	0.04	03:29:25.16	0.06	P
F. Casarramona	Spain	−2.0153	+36.8806	50	03:32:42.19	0.03	03:33:02.96	0.02	P
J. Ripero	Spain	−3.5806	+40.6429	648	03:29:01.40	0.20	03:29:23.40	0.30	P
P. Maley	Spain	−3.5581	+40.4485	610	03:29:11.89	0.10	03:29:31.10	0.10	P
F. Aceituno	Calar Alto, Spain	−3.3861	+37.0629	2896	03:32:18.7	–	–	–	M
				2017 October 9					
B. Leonard	Grandview, TX, USA	−97.1674	+32.2706	203	04:09:12.01	0.06	04:09:22.85	0.06	P
M. Smith	Grandview, TX, USA	−97.1675	+32.2706	203	04:09:11.98	0.03	04:09:22.78	0.03	P
J. Barton, R. Campbell	Clifton, TX, USA	−97.6713	+31.6755	298	04:09:23.63	0.01	04:09:33.60	0.01	P
D. Eisfeldt	Waco, TX, USA	−97.2499	+31.6291	161	04:09:23.34	0.03	04:09:31.18	0.03	P
R. Nugent	Dripping Springs, TX, USA	−98.1660	+30.1951	399	04:09:54.1	–	–	–	M

Notes. The longitude λ and latitude ϕ are geodetic coordinates, and h is the altitude above sea level. The disappearance and reappearance times are denoted by t_D and t_R, respectively, and their reported uncertainties by σ_D and σ_R. The observation type is P for a positive detection and M for a miss. A dash indicates that no value was reported.

Appendix E: Surface features

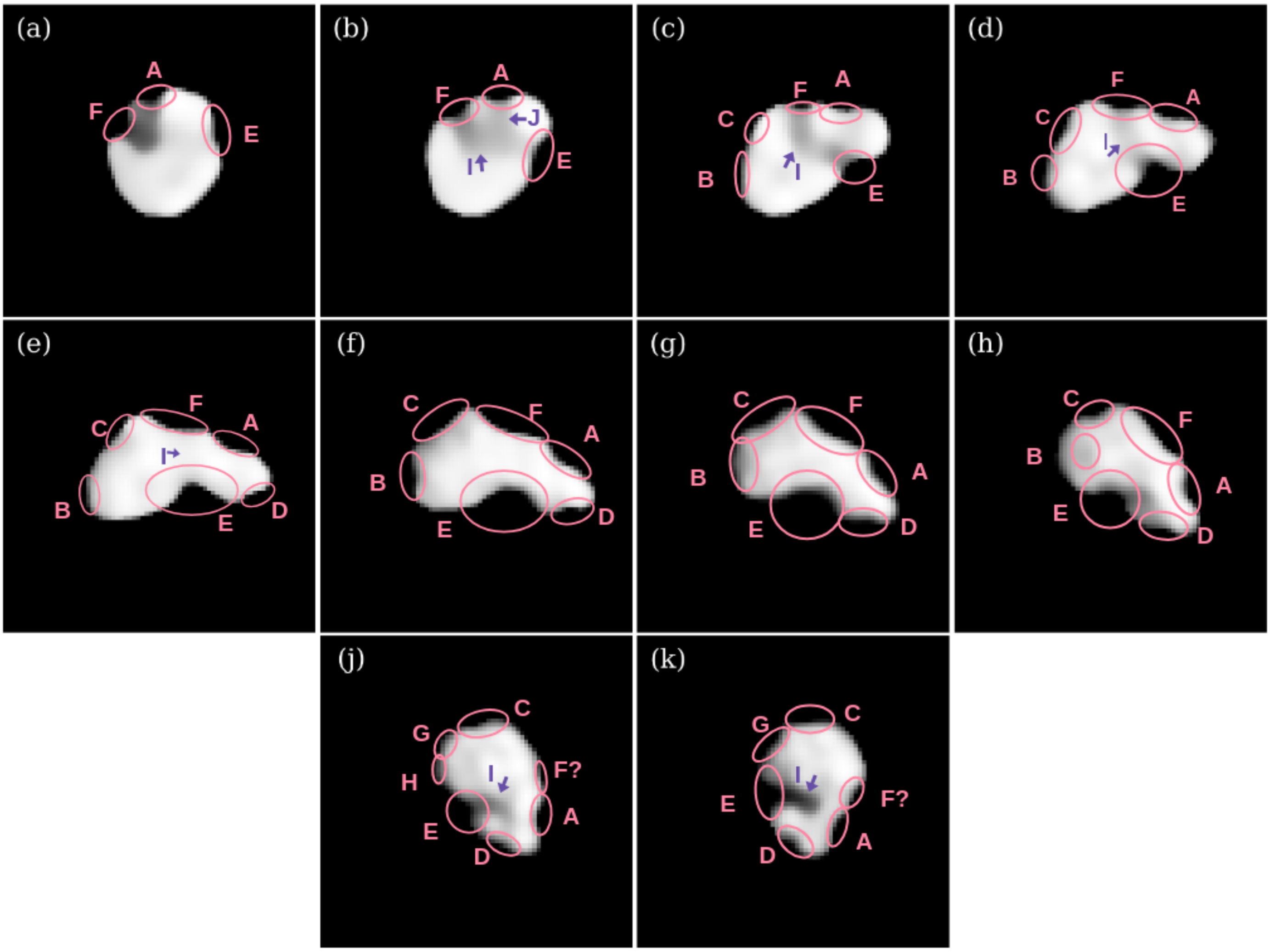

Fig. E.1. Surface features identified on Nysa in the 2026-02-15 SHARK-VIS dataset. Edge indentations are marked with pink ovals and shadowed features are marked with purple arrows. Each feature is marked with a corresponding Letter; the measured size and description of these features can found in table E.1.

Table E.1. Surface features of Nysa.

Feature	Type	Width (km)	Depth(km)
A	Crater/secondary basin	38	6
B	Crater	20	
C	Crater	35	
D	Crater	21	3
E	Southern cavity *	53	17
F	Northern cavity	44	5
G	Crater	17	
H	Crater	8	
I	Collum/Valley		
J	Collum/Valley		

Notes. Crater width and depth correspond to the maximum measured projected width and depth of a feature. Reported measurements correspond to the frame in which the largest cross-section of the feature was visible. Uncertainties for all reported values are one pixel, or 5 km. Depths are not reported for features with a depth less than two pixels. Indentations associated with a collum are denoted as basins, independent indentations are denoted as craters. Location of the features can be seen in Fig. E.1 and Fig. 1.
* Ambiguous edge